NATIONAL AIR INTELLIGENCE CENTER

SELECTED ARTICLES

19960903 012

HUMAN TRANSLATION

NAIC-ID(RS)T-0135-96   12 June 1996

MICROFICHE NR:

SELECTED ARTICLES

English pages: 29

Source: Qiangjiguang Yu Lizishu (High Power Laser and
         Particle Beams), Vol. 2, Nr. 4, November 1990;
         pp. 409-417, 461-466

Country of origin: China
Translated by: Leo Kanner Associates
                F33657-88-D-2188
Requester: NAIC/TATD/Bruce Armstrong
Approved for public release: distribution unlimited.

TABLE OF CONTENTS

GRAPHICS DISCLAIMER

All figures, graphics, tables, equations, etc. merged into this
translation were extracted from the best quality copy available.

Laser-induced Thermal Damage of Copper Reflecting Mirrors

Liu Chenghai, Yuan He and Pei Wenbing

(Institute of Applied Physics and Computational Mathematics, Beijing)

Abstract: A physical model for laser-induced thermal damage of optical surfaces has been developed and used to study damage thresholds, cooling and cumulative effects. The computed dependence of damage thresholds on laser pulse duration is in agreement with experimental and theoretical results reasonably. A concept about critical cooling thickness of mirrors has been suggested, and a scaling law of multi-pulse cumulative effects has been obtained.
Key Words: laser-induced thermal damage, copper reflecting mirror, damage threshold, critical cooling thickness, cumulative effect

1. Introduction

The effect of high-power laser-induced thermal damage on the surfaces of metal mirrors, semiconductors and other opaque dielectric optical materials serves as one of the leading laser damage mechanisms. A high-power laser, able to transport its energy within an extremely small space scale near the surface of the foregoing materials in a rather short time, can cause those materials to undergo a temperature rise, softening, melting, evaporation and even avalanche ionization. Technically, damage thresholds are related not only to laser wavelength, pulse width and material properties, but also impurities, defects and surface fineness of optical materials. Since factors like impurities, defects and surface fineness vary to a great degree and exhibit marked randomness, damage thresholds measured in the laboratory will accordingly show high dispersion. However, the hot-melt

1

damage of materials is "intrinsic" or "inherent". For many years, experimental and theoretical research was widely carried out on the effects of laser-induced thermal damage on optical surfaces [1-4].

A simplified physical model was established in this paper to study laser-induced thermal damage effects on optical surfaces. With this model, desirable results were obtained in the study of 1.06μm laser-induced thermal damage effects on copper reflector surfaces. Numerical computations were conducted over the relationship between laser melting damage threshold on copper reflector surface I_{th} and laser pulse width $\tau\rho$. The results showed that such relationship could satisfy a minus 1/2 power law $I_{th} \propto \tau_p^{-1/2}$, which well conforms to theoretical and experimental results. Also, the relationship between the melting threshold intensity on the copper reflector surface and the copper mirror thickness was studied under a given pulse width. The results indicated that when the copper mirror thickness is larger than a determined thickness related to pulse width, external cooling of the copper reflector can no longer raise the reflector melting damage threshold. This determined thickness was called critical the thickness of reflector back surface external cooling.

In addition, multi-pulse cumulative effect was also investigated. By irradiating a copper reflector with a multi-pulse laser lower than the monopulse damage threshold, the relationship between the number of pulses needed for cumulative damage and intensity of each pulse was acquired, which could approximately meet a power scaling relation $N_{th} \propto (I/I_{th})^{-2.1}$.

2. Physical Model

The simplified physical model developed contains a laser body distribution source, conduction-band electron absorption,

phase variation latent heat smoothing, heat transfer, and
reflector back surface cooling [5].

The heat transfer equation of laser body distribution source
can be expressed as:

$$\rho_0 c_p \frac{\partial T}{\partial t} = \frac{\partial}{\partial x} (k \frac{\partial T}{\partial x}) + S_L(x,t)$$

(2.1)

where P_0 is the reflector mass body density, C_p is the constant-
pressure specific heat, K is the reflector thermal conductivity,
$S_L(x,t)$ is the time correlation body distribution laser energy
source rate, and T(x,t) is the reflector temperature
distribution.

The mode of body distribution laser energy is

$$S_L(x,t) = (1-r) I_i(t) \alpha_c \exp(-\alpha_c x)$$

(2.2)

where $I_i(t)$ is the incident laser intensity, γ is the laser
reflectivity, α_c is the laser absorption coefficient of
conduction band electrons.

The laser waveform is single-gaussian type or multi-gaussian
type distribution

$$I_i(t) = \sum_i I_{0i} \exp \{ - \frac{(t-t_{pi})^2}{2\tau_{pi}^2} \}$$

(2.3)

where τ_{pl} and t_{pl} are, respectively, the laser pulse width and
laser peak time, I_{0l} is the laser peak intensity.

The absorption coefficient α_c is calculated from the
imaginary part of complex refractivity exponent of the reflector
material as follows:

3

$$\alpha_c = \frac{2\omega_L}{c} I_m(n) = \frac{2\omega_L}{c} n_i \tag{2.4}$$

where ω_L is the laser angular frequency, c is the speed of light in vacuo, n is the complex refractivity exponent, i. e.

$$n \equiv Re\,(n) + i\,Im(n) \equiv n_r + in_i \tag{2.5}$$

The imaginary part and the real part of the complex refractivity exponent, respectively, are:

$$n_r = [\frac{1}{2}(\gamma + \beta)]^{1/2} \tag{2.6}$$

$$n_i = [\frac{1}{2}(\gamma - \beta)]^{1/2} \tag{2.7}$$

Here

$$\beta \equiv \frac{1 - \omega_p^2}{\omega_L^2 + \nu_c^2} \tag{2.8}$$

where

$$\gamma \equiv [\beta^2 + (1 - \beta)^2 (\frac{\nu_c}{\omega_L})^2]^{1/2} \tag{2.9}$$

and

$$\omega_p = (\frac{4\pi n_e^2}{m_e})^{1/2} \tag{210}$$

$$n_e = \sum_\alpha n_\alpha Z_\alpha = \sum_\alpha N_0 P_\alpha Z_\alpha \tag{2.11}$$

is the conduction-band electron density, P_α is number of α-category atom grade, Z_α is α-category conduction band electrons.

$$\nu_c = \frac{\omega_p^2}{4\pi\sigma_0} \tag{2.12}$$

is the collision frequency, where σ_0 is the DC-current electroconductivity.

When the incident laser pulse is the single-gaussian type or multi-gaussian type distribution, the laser reflectivity will be

$$r = \frac{(n_r - 1)^2 + n_i^2}{(n_r + 1)^2 + n_i^2}$$

(2.13)

For the convenience of differential computations, discontinuous phase variation latent heat underwent smoothing processing. Let the constant-pressure specific heat be

$$c_p = c_{p0} + \frac{H_m}{(2\pi)^{1/2} \Delta T_m} \exp\left\{ -\frac{(T - T_m)^2}{2\Delta T_m^2} \right\}$$

(2.14)

where c_{p0} is the solid phase specific heat, T_m is the melting point, ΔT_m is the temperature interval during phase-variation latent heat smoothing, and H_m is the latent heat of melting.

3. Relationship between Melting Threshold and Pulse Width

By using this physical model, the melting damage thresholds of copper reflector surfaces were studied within a laser width range from ps to ms level. The study results are shown in Fig. 1.
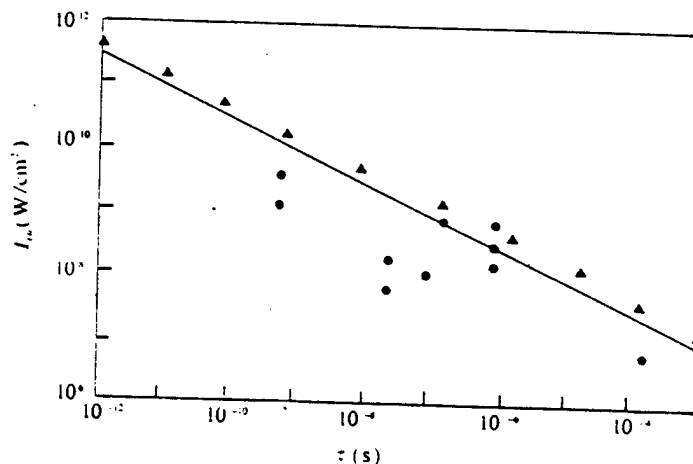

Fig. 1   Relationship between Pulse damage threshold and Pulse Width(copper, positive incident)

5

Figure 1 shows the relationship between copper reflector melting-damage thresholds and laser pulse widths. In Fig. 1, solid circular points "•" and the oblique straight line, respectively, stand for foreign experimental and theoretical results (data from different sources), suggesting the following:

$$I_{th} = 10^{10} \left(\frac{1}{\tau_p} \right)^{1/2} \qquad (W/cm^2) \qquad (3.1)$$

reciprocal 1/2 quadratic scaling relations between melting damage threshold and pulse width [7]. Here, τ_p is measured with s as unit, solid triangles "▲" represent our numerical computations. For the convenience of comparison, the reflectivity adopted in our numerical computations was the same value as that in the foreign theoretical calculations given in the figure, i.e. $\gamma = 0.992$; also in the figure, $\tau_p = 30ps$ is equivalent to free-electron laser micropulse width.

It can be seen from Fig. 1 that our numerical computations well conform to overseas theoretical calculations. Experimental results showed the same pulse-width scaling relation, with experimental points lower than the theoretical and numerical computations in most cases. It is not strange to find some difference between the experimental results and theoretical, numerical, results, since what is given here refers to melting damage thresholds, and melting damage, as mentioned in the Introduction of this paper, is "intrinsic", i.e. it is determined solely by material melting, without considering all non-intrinsic factors such as material impurities, lattice defects, surface contamination and environment effects. Such ideal conditions can be adopted in theoretical and numerical computations, yet it is impossible to rule out all non-intrinsic factors in experiment. Therefore, it is not strange that the experimental damage

6

thresholds exhibit lower values and some dispersion compared with theoretical and numerical computations that are obtained under the foregoing ideal conditions.

It is not difficult to comprehend the reciprocal 1/2 quadratic relationship between the reflector melting damage threshold and the laser pulse width. From the energy balance relationship, the following can be obtained:

$$(1-r)\tau_p I = \rho c_p \Delta_x \Delta T \tag{3.2}$$

where I is the laser intensity, Δ_x is the heat transfer depth, is the average temperature rise of reflector. Based on thermal conductivity, the heat transfer depth can be estimated as $\overline{\Delta T}$

$$\Delta_x \approx \left(\frac{4\tau_p k}{\rho c_p} \right)^{1/2} \tag{3.3}$$

and the average temperature rise of the reflector can be estimated as

$$\overline{\Delta T} = \frac{1}{\Delta_x} \int_0^{\Delta_x} (T-T_0)\,dx \approx \frac{1}{2}(T_m-T_0) \tag{3.4}$$

where T_m is the melting point. Then, the melting damage threshold can be estimated as

$$I_{th} \approx \frac{1}{2} \frac{(4\rho c_p k)^{1/2}}{(1-r)}(T_m-T_0)\tau^{-1/2} \tag{3.5}$$

For copper, ρ=8.9 g/cm^3, c_p=0.39 J/K•g, linear thermal conductivity is k=4J/cm•s•K, T_m=1356K. Let T_0=300K and γ=0.992, then

$$I_{th} \approx 1.56 \times 10^{10} \left(\frac{1}{\tau_p} \right)^{1/2} \quad (\mathrm{W/cm^2}) \tag{3.6}$$

where τ_p is measured with s as unit. This rough estimate agrees with theoretical threshold semi-quantitative value.

7

4. Relationship between Melting Damage Threshold and Reflector Thickness

The relationship between damage threshold and reflector thickness under external cooling of the reflector back surface was studied. In our physical model, "intensive cooling", i.e. cooling water was taken as a constant temperature, and cooling water can effectively carry away energy that reaches the back of the reflector so that the reflector back can maintain a constant temperature.

Fig. 2 shows such computations. In this computation example, the laser pulse width is $\tau=1ms$. It can be seen that when the reflector thickness is less than d, i.e. d<1mm, the reflector melting damage threshold rises rapidly with decrease in reflector thickness, with a scaling relationship approximately as:

$$I_{th} \propto d^{-1}$$

(4.1)

However, if the reflector thickness surpasses d, i.e. d>1mm, reflector damage threshold remains to be a constant, independent of its thickness, which suggests that for metal reflectors with d>1mm, external cooling of reflector back surface can not increase the laser melting damage threshold with its pulse width at ms order, i.e. in this case, the energy that the laser deposits in the reflector has not enough time to transfer to its back and therefore, cooling water can not carry away heat from the reflector back, i.e. cooling is factually ineffective.
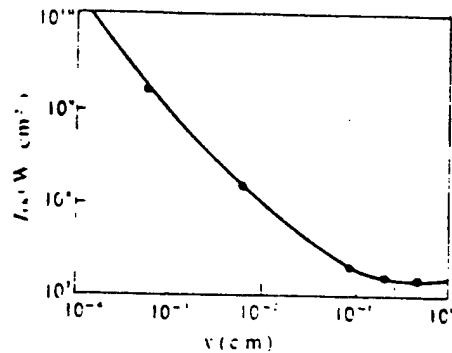
Fig. 2. Relationship between single damage threshold of target back surface cooling and target thickness (copper, positive incident, pulse width 1ms)

For laser with pulse width $\tau_p \approx$ ms, foregoing typical thickness d≈mm might as well be called the cooling critical thickness, which is just the heat transfer depth in linear heat conductivity theory. Thus, cooling is ineffective when the reflector thickness is larger than such critical thickness while it is effective when reflector thickness is smaller than critical thickness and furthermore, the thinner the reflector, the better cooling effect can be.

This cooling critical thickness d_c is related to reflector material properties and laser pulse width τ_p. Its value can be estimated as:

$$d_c \approx (\frac{4k\tau_p}{\rho c_p})^{1/2}$$

(4.20)

For pulses τ_p=1ms, $d_c \approx$0.68mm, which conforms well to the foregoing calculations.

9

5. Multi-pulse Cumulative Effect

In studying multi-pulse cumulative effect, the single laser pulse width was taken as $I_{th}=1/5 \times 10^{10} W/cm^2$, and as mentioned above, the single-laser pulse damage threshold over the copper reflector is $I_{th}=1.5 \times 10^{10} W/cm^2$. To study the multi-pulse cumulative effect, the copper reflector was irradiated with multi-pulses with a pulse interval t_p and an intensity lower than the single pulse damage threshold. As the intensity of each single pulse in such pulse train is lower than the damage threshold, any pulse can not cause damage effects on its own, but damage will be caused only when the number of pulses has accumulated such that the cumulative effect is builds up. We introduced a normalized intensity that is equal to the single pulse intensity divided by the single pulse damage threshold. Fig. 3 shows the relationship between the number of pulses needed for the cumulative effect and normalized laser intensity.
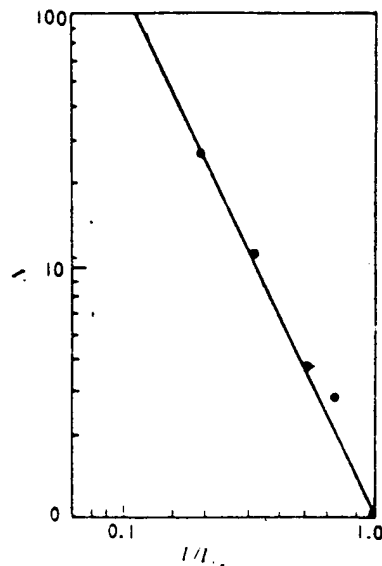

Fig. 3. Relationship between number of pulses needed for cumulative effect and normalized intensity (copper, positive incident, damage threshold $1.5 \times 10^{10} W/cm^2$ of single pulses with pulse width 1ns and pulse interval 5ns)

It can be seen that Fig. 3 approximately satisfies the power law

$$N_{th} \approx (\frac{I}{I_{th}})^{-2.1}$$

(5.1)

where I_{th} is the single pulse damage threshold, I is the intensity of each single pulse in a multi-pulse laser, N_{th} is the number of pulses needed for the cumulative effect. For instance, if the intensity of each pulse in a multi-pulse laser is $I/I_{th}=0.6$ times the single pulse damage threshold, then the number of pulses needed for the cumulative effect will be $N_{th}=3$; and if the intensity of each pulse in a multi-pulse laser is $I/I_{th}=0.1$ times the single-pulse damage threshold, then $N_{th}=125$, which is obviously an extremely strong scaling relationship. Of course, since multi-pulse types are very much diversified, it is impossible for all multi-pulse types to obey the same law. Eq. (5.1) was derived for pulse width $\tau_p=1ns$ and pulse interval $t_p=5ns$. Currently, our research on multi-pulse cumulative effect is ongoing.

6. Conclusions

We developed a simplified physical model of laser-induced thermal damage effect on metal reflectors. With this model, numerical computations were made and some helpful results were acquired, which include the following aspects:

1. A reciprocal 1/2 quadratic power scaling relationship was derived between laser-induced damage threshold on copper reflectors and laser pulse width, which conforms well to theoretical and numerical computations.

2. A concept of reflector critical thickness of its back surface external cooling was proposed and its semiquantitative results

11

were given.

3. A scaling relationship concerning the multi-pulse cumulative effect was derived.

References

[1] M.Law, J.Bender and C.K.Carniglia. Laser induced Damage in Optical Materials. NIST SPECIAL PUBLICATION 752, Boulder, Colarado, U.S.A..532.(1986).

[2] D.J.Gallant, A.F.Steward, Nat.Bur.Stand.(U.S.) Spec.Publ.727, 272.(1984).

[3] Y.M.Xiao, et al., $Appl.Opt.$ 22, 2922 (1983).

[4] P.A.Temple, W.H.Lowdermilk and D.Milam, $Appl.Opt.$, 21, 3249 (1982).

[5] 刘成海、袁河、裴文兵、激光对光学材料表面热破坏效应的简化物理模型, 应用物理与计算数学研究报告, 1988年.

[6] A.Edwards, et al. UCRL-51489.

[7] 刘成海、强激光与材料相互作用和损伤破坏机理、应用物理与计算数学研究报告、1987年.

Experimental Studies of Stimulated Raman Scattering

Mei Qiyong, Zhao Xuewei, Zheng Zhijian, Tang Daoyuan and Peng Hansheng

(Southwest Institute of Nuclear Physics and Chemistry)

Abstract: The scaling relations between the energy of stimulated Raman scattering (SRS) and that of incident laser light for a few target configurations are experimentally investigated. The generation condition and evolution of SRS is revealed. The results show that SRS in blackbody targets is the dominant mechanism to generate suprathermal electrons. The SRS spectra vary from 1.2 to 2.1µm and the anti-Stokes light generated by 1.053µm laser light is observed. From the short wavelength cutoff of the SRS spectra we find that the electron temperature in the plasma corona is 1.35keV. Additionally, by using the spectra we find that SRS occurs in an electron density region from 0.07 to $0.15n_c$, with its peak at $1.5 \times 10^{20}/cm^3$.

Key Words: stimulated Raman scattering, two-plasmon decay change, resonance absorption, suprathermal electron.

1. Introduction

Stimulated Raman scattering (briefly SRS) has attracted growing attention from theoretical and experimental workers [1-6] in experimental research on initial constrained fusion (briefly ICF). The reason is that SRS, in dissipating a large amount of laser energy and producing extremely high energy suprathermal electrons, directly affects plasma absorption of laser energy and effective compression of high-gain target nuclei, as well as affecting our understanding of the explosive process inside the target nucleus, thus leading to complexity in theoretical analysis. In addition, since SRS conveys large amounts of

information on the interaction between laser light and plasma, it can help us to gain an insight into this interaction and allows us to derive the plasma electron temperature and electron density. Therefore, laboratories with large scale laser devices started SRS experimental research from the seventies, particularly Lawrence Livermore National Laboratory (LLNL), the KMS Fusion Company and the University of Rochester, which made outstanding achievements. In the past ten years, these laboratories carried out research on the SRS properties of thick disk targets and film targets, made of various materials, with 10.6μm CO_2 laser light, 1.06μm rubidium glass laser light and its frequency multiplier light (with wavelengths of 0.53 and 0.35μm) respectively. Also, the SRS properties of cavity targets were studied with 0.53μm laser light at the Laser Engineering Institute, Osaka University, Japan.

SRS is a significant interaction process between laser light and plasma, during which incident laser light is converted to an electron plasma wave and a scattering light wave. Both waves can satisfy frequency and wave-vector matching

$$\omega_0 = \omega_{epw} + \omega_s \tag{1}$$

$$k_0 = k_{epw} + k_s \tag{2}$$

where ω_0, k_0; ω_s, k_s; ω_{epw}, k_{epw} respectively are incident laser light, and SRS and electron plasma frequencies and wave vectors. Their dispersion relations can be expressed as

$$\omega_0^2 = \omega_p^2 + k_0^2 c^2 \tag{3}$$

$$\omega_s^2 = \omega_p^2 + c^2 k_s^2 \tag{4}$$

$$\omega_{epw}^2 = \omega_p^2 + 3 k_{epw}^2 v_{th}^2 \tag{5}$$

14

where $\omega_p^2 = 4\pi n e^2 / m_e$ is plasma frequency; c is the velocity of light; $v_{th} = (k_B T_e / m_e)^{1/2}$ is electron thermal velocity; k_B is Boltzmann constant; e, m_e, T_e and n respectively are electron charge, mass, temperature and density. In nonuniform plasma, matching conditions can be met within the range below $n_c/4$.

$n_c = m_e \omega_0^2 / 4\pi e^2$ is the critical density of incident laser light, whose lower boundary is determined by intensive Landau damping. Electron plasma waves generated in the SRS process can create harmful suprathermal electrons due to Landau damping, and as a result, the SRS light escapes from the plasma with laser energy.

SRS energy and energy spectrum are closely associated with incident laser light wavelength, energy and pulse width as well as target material, shape, and scale. The aim of SRS research is to determine its generation conditions and evolution regularities so as to suppress it, restrict its growth, or use it to obtain some specific information concerning the relationship between laser light and plasma.

In recent years, the SRS of plane targets and several blackbody targets was measured with 1.053μm laser light on the "Wonderful Light" computer at Shanghai United Laser Laboratory. As a result, we found the interdependent relations between the SRS light portion and incident laser energy; the interdependent relations between SRS light energy and plasma scale; backward Stokes and anti-Stokes spectra in the backward direction, as well as the plasma electron temperature deduced from the SRS spectrum short-wave cutoff, and the plasma electron density from the spectral distribution. By comparing SRS, anti-Stokes, $2\omega_0$ and $3\omega_0/2$ spectral intensities, we concluded that backward SRS in blackbody targets was the main mechanism for generating suprathermal electrons and also we arrived at a tentative knowledge of the SRS generation conditions and its evolution

regularities.

Basically, interaction between 1.053μm wavelength laser light and plasma generates SRS light with a wavelength range from 1.20 to 2.12μm in the backward direction. However, it is rather difficult to measure spectra within such a range, because at wavelengths longer than 1.0μm and photon energy below 1eV, it becomes insensitive to detectors, which are otherwise sensitive to visible light and near-infrared light. In that case, measurements have to depend on indium arsenide or thermovoltaic detectors, which are quite expensive and extremely demanding in use. This situation obviously affects its research. So far, to our best knowledge, only LLNL has conducted measurements on SRS spectra with such a waveband range by using a separated indium arsenide detector on the Argus facility, and a 24-unit indium arsenide detector array on the Shiva facility.

2. Experiment Arrangements and Measurements

The experiment was undertaken on the "Wonderful Light" computer at Shanghai United Laser Laboratory. During the experiment, the laser light used had a wavelength of 1.053μm, Gaussian pulses with a waveform of approximately 1ns (FWHN) and energy in the range of 60 to 600J; the power density at the target surface varies generally from 5×10^{14} to 5×10^{15}W/cm^2, with variation in laser energy, pulse width and focal spot scale. Passing through a ø~60+1/2μm target focusing lens, the laser light was focused on various targets in the form of focal spots, where 1 is distance of the target surface from focusing. SRS is generated following the interaction between the laser light main peak and the plasma produced during interaction between the laser light leading edge and the target surface. In that case, the SRS energy and energy spectrum were observed in the backward direction. The overall arrangements of the experiment are shown in Fig. 1.
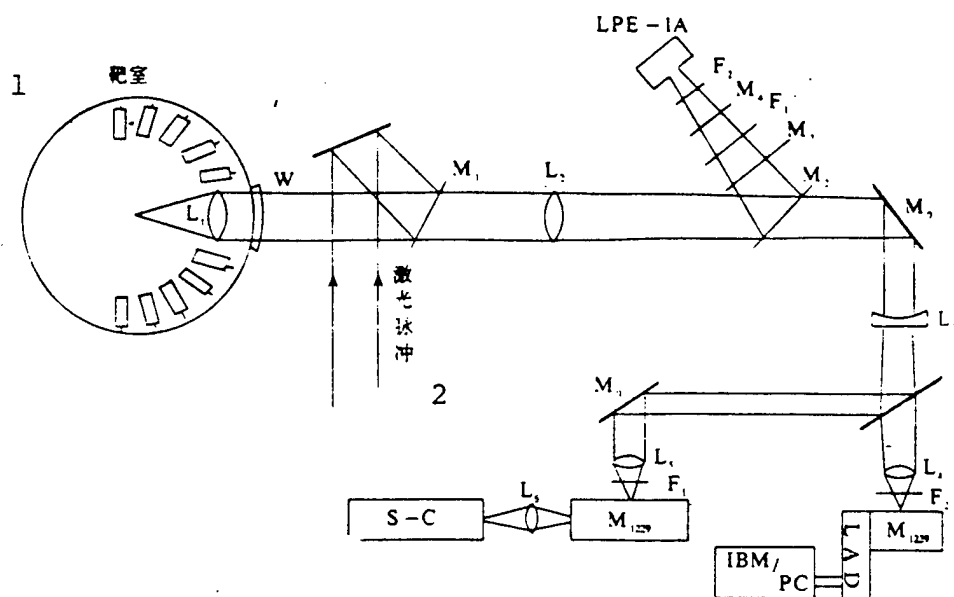
Fig. 1. Schematic diagram of experiment overall arrangements

L_1--f/1.7 targeting lens; W--target window; M_{1-5}--1.06μm reflector; L_2--f=2.8m condenser lens; F_1--neutral attenuation film; F_2--infrared high-pass optical filter; M_0--aluminum total reflector; L_3--f=-10cm negative lens; L_4, L_5, L_6--f/38 focal lens group; ☐ --Photodiode; M_{1229}--Czerny-Turner spectrometer; LAD--array detectors; IBM-PC--computer

Key: 1. Target chamber; 2. Laser pulse

SRS energy was measured with an LPE-1A laser power/energy meter. SRS light, generated by interaction between laser light and plasma, was collected by the f/1.7 targeting lens and converged on calorimeter with the L_2 lens. M_1, M_3 and M_4, located on the optical path, are three 1.06μm total-internal reflectors, which are used to ensure that SRS measurements are not interfered by mirror reflection with a wavelength close to 1.06μm, as well as stimulated Brillouin scattering (SBS). F_1 and F_2 are infrared high-pass optical filters, whose transmissivity is ≥70% to SRS light with a wavelength ≤1.2μm and its transmissivity <1% to light with a wavelength ≤1.0μm and which are used to ensure that $2\omega_0$ and $3\omega_0/2$ harmonic waves do not interfere with SRS measurements. Both of them in combination can ensure SRS light purity and a satisfactory signal/noise ratio.

The backward SRS spectrum was measured with a 0.25m raster spectrometer and a 128 unit thermovoltaic array detector with a spectrum resolution better than 15nm.

Anti-Stokes light was measured with a 0.25m raster spectrometer and CCD-1024 silicon array detector with a spectrometric resolution better than 1nm.

Among the targets involved were thick gold disk targets and blackbody targets of different standards. The gold disk targets were 20μm thick, with two kinds of focal spot scales: 20μm, and ø~60μm and ~210μm. The blackbody targets had the first incident surface ø~210μm and a vacant cavity scale ranging from ø300 to 800μm.

3. Experimental Results

In the case when the laser energy was lower than 50J, the SRS energy in thick gold and aluminum disk targets was approximately at the microjoule level and fluctuated to a great degree, which suggests that unstable SRS is caused by its location near the threshold.

In large-scale blackbody targets, SRS energy increases exponentially with increase in laser energy, which indicates a distinct stimulated character as shown in Fig. 2. It can be seen from the figure that the SRS threshold in medium-scale blackbody targets is approximately 30J, and its energy is approximately 1J while the laser energy is 50J, which suggests a dramatic increase of SRS compared with that in thick disk targets. This indicates that SRS buildup development is related not only to laser power density but, more importantly, to plasma scale. When laser energy reaches 400J, the SRS fraction in medium scale blackbody targets is around 8% of the incident laser energy, which proves to be a rather larger SRS fraction than ever before measured in

the laboratory. On the whole, SRS increase does not exhibit a saturation tendency under present conditions. The conditions under which SRS will reach saturation is of concern in both experiment and theory.
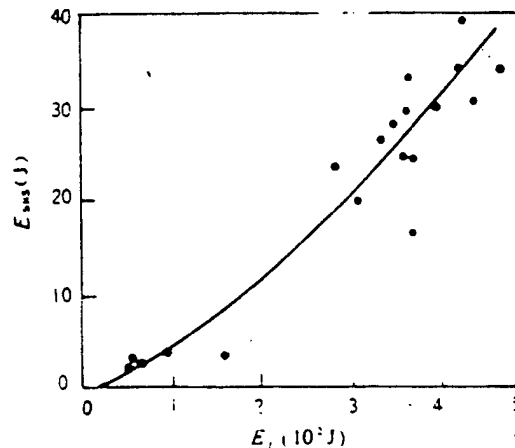

Fig. 2. Interdependent relations between SRS energy (E_{SRS}) and incident laser energy (E_L) in medium scale blackbody targets

Fig. 3 shows the interdependent relations between SRS light energy and plasma scale. It can be seen from Fig. 3 that there are significant interdependent relations between SRS energy and plasma scale. When laser energy remains basically unchanged, SRS energy rapidly increases with the increasing plasma scale within the range of 340-380J. The SRS energy in gold disk targets with focal spots ø210μm increases to nearly 20 times that in gold disk targets with focal spots ø60μm. Under the same focal spots, the SRS energy in medium-scale blackbody targets is over ten times higher than that in gold disk targets. It can also be seen from the figure that when the blackbody target scale keeps increasing, SRS energy increases slowly. It can be conceived, then, that once the blackbody target scale increases to a certain value, SRS energy will probably start to decrease because overly large cavities can not confine the plasma, which shows no difference from that in gold disk targets.
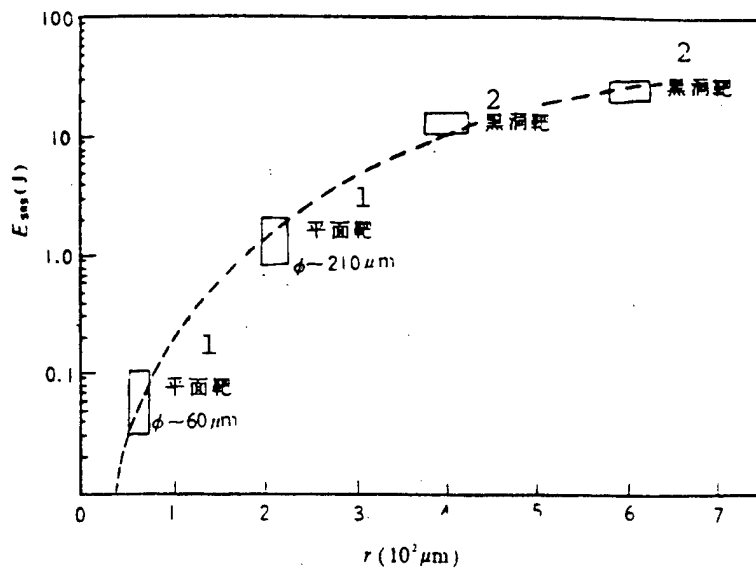
Fig. 3. Interdependent relations between SRS
energy (E_{SRS}) and plasma radial scale r ($10^2\mu m$)
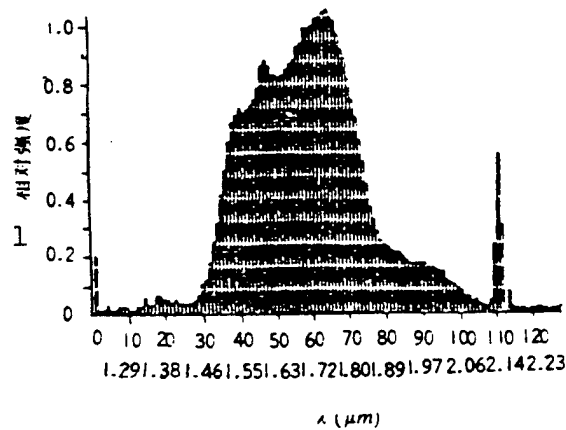
Key: 1. Plane target; 2. Blackbody target

Fig. 4. Typical backward SRS time integral
spectrum in blackbody targets
Peak with a wavelength 2.14μm is dipole spectrum
of light with a wavelength 1.06μm

Key: 1. Relative intensity

Fig. 4 shows a typical backward SRS time integral spectrum
in blackbody targets. The laser energy on the target is 383.7J,

FWHM 1096ps, focal spot ø~210μm and target cavity is medium scale. It can be seen from the figure that the spectrum wavelength ranges from 1.46 to 2.06μm, the peak is located at 1.77μm, the FWHM is 350nm, short-wave end swiftly decreases, and the cutoff wavelength is 1.46μm. At the same time, long-wave end decreases slowly and extends up to 2.10μm. Noticeably, the small peak at 2.14μm is not the SRS peak corresponding to $n_c/4$ region, but the dipole spectrum of SRS and 1.06μm reflected laser light, which is specially added as a wavelength identification spectrum. This peak will disappear as long as one more 1.06μm total-internal reflector or infrared high-pass optical filter is placed in front of the spectrometer or on the optical path, which further proves that the peak with a 2.14μm wavelength is an 1.06μm light dipole spectrum instead of SRS light. Because neither a 1.06μm reflector nor an infrared high-pass optical filter can block light with 2.14μm wavelength but it can hinder 1.06μm light.
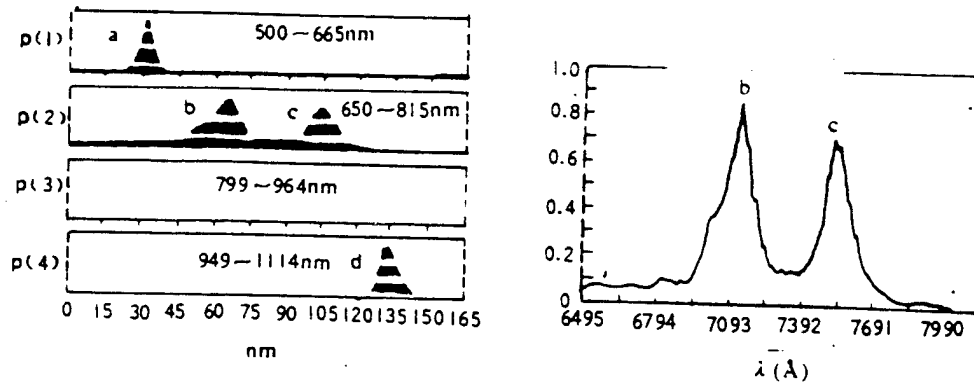
Fig. 5. Scattering spectra detected in blackbody targets with a 0.25m raster spectrometer and CCD-1024 array detectors

At left is the overall figure: (a)$2\omega_0$; (b)$3\omega_0/2$; (c)anti-Stokes (d)ω_0

At right is enlarged $3\omega_0/2$ harmonic wave and anti-Stokes spectrum with wavelength identification

(c) in Fig. 5 is a typical anti-Stokes spectrum in blackbody targets. The figure at the left is an overall figure, where (a) is the $2\omega_0$ harmonic wave with center wavelength 530nm; (b) is $3\omega_0/2$ harmonic wave with center wavelength 710nm; (c) is the anti-Stokes spectrum with center wavelength 750nm; (d) is SBS light with wavelength 1.06μm and specular reflection spectrum. The figure at the right is enlarged (b) and (c) spectra with wavelength identification. Because SRS light, $3\omega_0/2$ light and anti-Stokes light are all more intense than $2\omega_0$ light in blackbody targets, to display all the four different intensity lights on the screen, we respectively added an 1.06μm total-internal reflector and a $2\omega_0$ high-pass optical filter in front of the spectrometer so as to make the $3\omega_0/2$ and anti-Stokes intensities one order lower than that of $2\omega_0$, and to reduce ω_0 by a factor of more than 1,000. It was then deduced that the $3\omega_0/2$ harmonic wave intensity was of the same order as the anti-Stokes light, approximately one order lower than $2\omega_0$, while the anti-Stokes light was only a small fraction of the SRS light. It was further found that the SRS intensity in blackbody targets was much larger than that of $3\omega_0/2$ and $2\omega_0$ harmonic waves.

4. Results and Discussion

Comparison between SRS energy and that of $2\omega_0$ and $3\omega_0/2$ shows the following: (1) $2\omega_0$ and $3\omega_0/2$ harmonic wave energy is not larger than that of SRS in gold disk targets with focal spot $\varnothing \lesssim 60$μm as shown in Table 1, which suggests that two-plasmon decay change (TPD) and resonance absorption (RA) are major physical processes in disk targets with small focal spots; (2) SRS energy starts to exceed that of $2\omega_0$ and $3\omega_0/2$ in gold disk targets with focal spot $\gtrsim \varnothing 210$μm, which indicates that the SRS process already surpasses TPD and RA processes and begins to play an important part and (3) SRS energy has greatly exceeds that of $2\omega_0$ and $3\omega_0/2$

in medium scale blackbody targets, indicating that the SRS
process greatly exceeds TPD and RA processes to become a major
physical process.

Table 1   SRS, $2\omega_0$ and $3\omega_0/2$ Energy in Various Targets (incident
laser energy 340-380J)

1 靶 型	2 焦 斑 (μm)	E_{SRS} (J)		$E_{2\omega_0}$ (J)		$E_{3\omega_0/2}$ (J)	
		3 范 围	4 平 均	3 范 围	4 平 均	3 范 围	4 平 均
5 金盘靶	∅60	0.03 ~ 0.11	0.06	0.10 ~ 0.38	0.27	0.23 ~ 0.68	0.32
	∅210	0.3 ~ 2.1	1.10				
6 黑洞靶	∅210	10 ~ 15	13.0	0.4 ~ 0.8	0.6	1.6 ~ 1.8	1.7

Key: 1. Target type; 2. Focal spot; 3. Range; 4. Average;
5. Gold disk target; 6. Blackbody target

It can be seen even more clearly from Fig. 6 that SRS serves
as a major process at any time in blackbody targets; even if the
incident laser energy ranges from 50 to 100J, SRS energy still
considerably surpasses that of $2\omega_0$ and $3\omega_0/2$ harmonic waves.
Therefore, it is definite that SRS plays a dominant part at any
time in blackbody targets and serves as a major mechanism for
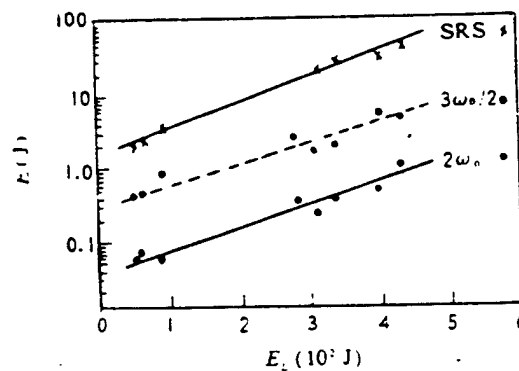generating suprathermal electrons.

Fig. 6. Interdependent relations between SRS,
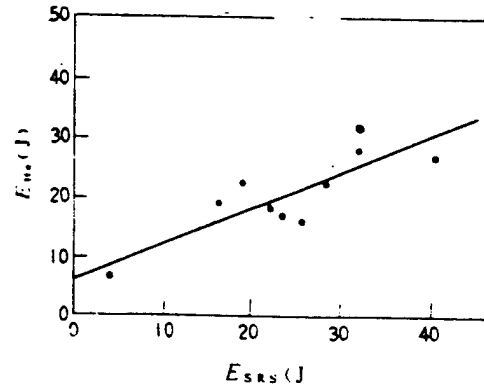$2\omega_0$, $3\omega_0$ energy and incident laser energy in
blackbody targets

Fig. 7. Interdependent relations between SRS
energy (E_{SRS}) and suprathermal electron energy (E_{He})

A comparison between SRS energy and suprathermal electron energy can exhibit their perfect interdependent relations as shown in Fig. 7, which can further demonstrate, from the energy conservation principle, that the major mechanism of producing suprathermal electrons in blackbody targets is SRS. Interestingly, when laser light in plasma decays to a scattering light in plasma, it can at the same time generate an electron plasma wave, which, through Landau damping or "wave breakage", generates suprathermal electrons. Thus, if the SRS process is the only process or is the major process that produces suprathermal electrons in blackbody targets, there should be well-defined interdependent relations between SRS energy and suprathermal electron energy. On the contrary, if the SRS process is not the major process that generates suprathermal electrons, there should not be well-defined interdependent relations between them. According to both theory and experiment, in the interaction process between laser light and plasma, several processes may create suprathermal electrons. For instance, the TPD process produced in $n_c/4$ region and RA process formulated in the n_c region may both stimulate electron plasma waves and generate suprathermal electrons. If the major mechanism of generating suprathermal electrons in blackbody

24

targets is TPD and RA processes instead of the SRS process, then there should not be well-defined interdependent relations between suprathermal electron energy and SRS energy. Nevertheless, the experiment shows that they do exhibit well-defined interdependent relations, which convincingly proves that SRS is the major mechanism of producing suprathermal relations in blackbody targets.

So far, we have verified that SRS is the major mechanism of generating suprathermal electrons with three arguments, namely the intensity and energy of SRS, $2\omega_0$ and $3\omega_0/2$, and interdependent relations between SRS and suprathermal electron energy. This provides vital information in solving the suprathermal electron problem.

Why does the SRS process become the major mechanism generating suprathermal electrons in blackbody targets? Because in blackbody targets, the plasma in cavities gives rise to, due to repeated laser light reflections in cavities as well as due to the confinement of cavities over plasmas, gives rise to a corona zone of large scale and uniform density. In this zone, the rather high density gradient ($L=ndx/dn$), favorable for SRS and SBS development, causes the SRS to intensify, and the intensified SRS and SBS can cause propagating laser light to lose a large amount of energy. When laser light passes through the large scale corona zone and arrives at the $n_c/4$ region where TPD is generated and the n_c region where RA is formed, its energy has already been greatly reduced. Accordingly, TPD and RA processes are suppressed, and with the increasing scale of the sub-$n_c/4$ region and the density gradient, SRS becomes more and more intensified. When the scale of the sub-$n_c/4$ region and the density gradient has increased to a certain value, SRS will surpass TPD and RA processes in absolute predominance and become the major mechanism generating suprathermal electrons.

In Fig. 4, the SRS time integral spectrum exhibits an extremely sharp short-wave cutoff, generally believed to be caused by Landau damping [7, 8]. Therefore, it can be used to find the plasma electron temperature in the corona zone. Theoretically, when $k_{ep}\lambda_D \geqslant 1/3$, intensive Landau damping is believed to be enough to suppress SRS growth in low density regions, where $\lambda_D = [T_e/4\pi ne^2]^{1/2}$ is Debye length, k_{ep} is the number of waves of electron plasma. When $k_{ep}\lambda D \ll 1$, k_{ep} can approximately be expressed as:

$$k_{ep} \approx \frac{2\omega_0}{c}\sqrt{(1-n/n_c)(1-\sqrt{n/n_c}+\frac{1}{4}n/n_c)}$$

(6)

By using SRS matching conditions (1) and dispersion equation (5), the plasma electron temperature in corona zone T_e can be solved through Landau damping criterion $k_{ep}\lambda_D \geqslant 1/3$ and repeat iteration. The SRS spectrum which corresponds to Fig. 4 has a short-wave cutoff wavelength 1.46µm. With foregoing methods, the plasma electron temperature was measured as T_e=1.35keV.

When the temperature is determined, relations between SRS intensity and plasma electron density can be obtained on the basis of relations between SRS spectrum intensity and wavelength. The typical SRS spectrum that corresponds to Fig. 4 generates SRS densities ranging from 0.07 to $0.19n_c$, i.e. $7\times10^{19}/cm^3$ to $1.9\times10^{20}/cm^3$, and the density corresponding to the peak value is $1.5\times10^{20}/cm^6$.

The experimental value of the backward SRS spectrum (Fig. 4) proves to be substantially different from what is predicted theoretically. Theory predicts that SRS is most likely to take place in the $n_c/4$ region, where it can most easily meet matching conditions, and there is the lowest threshold, the largest phase velocity of electron plasma waves and the smallest Landau

damping, etc. Nevertheless, the corresponding SRS light at wavelength $2\lambda_0$ has never been observed either in our experiment or in many overseas experiments. There might be two reasons for this: the first reason is that the incident laser dynamic force causes the $n_c/4$ interface to become steep and then to minimize the density gradient scale of that region ($L=ndx/dn$), thus hindering the generation of SRS; the second reason is that the $n_c/4$ region, due to its large size, can produce intensive SRS and SBS, for which incident laser light becomes extremely weak while arriving at this region. Both factors may suppress SRS generation and intensification in the $n_c/4$ region.

Peak (c) in Fig. 5 is believed to be anti-Stokes peak since, firstly, the wavelength (frequency) is suitable; secondly, the intensity is equivalent. By definition

$$\omega_s=\omega_0-\omega_{epw} \tag{7}$$

$$\omega_{A-S}=\omega_0+\omega_{epw} \tag{8}$$

where ω_s and ω_{A-S}, respectively, are SRS frequency and anti-Stokes light frequency. By adding the two equations, we obtain

$$\omega_{A-S}=2\omega_0-\omega_s \tag{9}$$

Experiment shows that in most blackbody targets, the Stokes light wavelength ranges from 1.46 to 1.90µm, and its corresponding frequency--from 0.73 to 0.53ω_0, while the anti-Stokes light frequency should be in the range 1.27-1.47ω_0 according to Eq. (9) and its corresponding wavelength should be 720-830nm. Incidentally, the peak (c) wavelength in blackbody targets was measured experimentally as 725-780nm, i.e. conforming to what is expected theoretically.

Fig. 5 also indicates that spectrum (c) shows the same intensity as spectrum (b), while spectrum (b) is the $3\omega_0/2$ harmonic spectrum, whose intensity is approximately 1/10 that of SRS. Thus, the anti-Stokes light intensity should also be 1/10 that of SRS, i.e. in agreement with LLNL measurements.

5. Conclusions

The foregoing measurements on relations between SRS energy and incident laser energy and target types yielded the SRS generation conditions and evolution regularities. Additionally, they proved that the SRS energy on gold and aluminum disk targets is in the order of microjoules when incident laser energy is less than 50J, suggesting a dramatic SRS increase in blackbody targets. In addition, it was demonstrated that, by comparison between SRS energy and $2\omega_0$, $3\omega_0/2$ and suprathermal electron energy, the major mechanism of generating suprathermal electrons in gold disk targets with focal spot $\varnothing \lesssim 60\mu m$ is TPD, RA and IPD, while SRS becomes a significant mechanism of generating suprathermal electrons in gold disk targets with focal spot $\varnothing \gtrsim 210\mu m$ and a major mechanism of its kind in medium scale blackbody targets. In blackbody targets, when the incident laser energy reaches 400J, SRS energy can arrive at over 30J, accounting for approximately its 8%, which is a rather larger fraction than has ever been observed in the laboratory. With a 0.25m raster spectrometer and 128 unit thermovoltaic array detectors, $1.053\mu m$ laser SRS spectrum was measured within a waveband range $1.2-2.2\mu m$. From spectrum short-wave cutoff, the plasma electron temperature was deduced as 1.35keV. It was also deduced from spectrum intensity distribution that SRS is basically formed within the range $0.07-0.19n_c$ in blackbody targets with most probable density $0.15n_c$, i.e. $1.5\times10^{20}/cm^3$. With a 0.25m raster spectrometer and CCD-1024 silicon array detectors, measurements were made at the same time on $2\omega_0$, $3\omega_0/2$ and anti-Stokes spectra, which provided vital information for comparison among the mechanisms of generating suprathermal electrons in blackbody targets. And finally, measurements on anti-Stokes spectrum were conducted in the backward direction, which provided helpful information for studying the mechanism of generating anti-Stokes light.

References

[1]   D. W. Phillion, D. L. Banner, E. M. Campbell, R. E. Turner, and K. G. Estabrook, *Phys. Fluids.* **25**, 1434 (1982).

[2]   W. L. Kruer, K. G. Estabrook, B. F. Lasinski, and A. B. Langdon, *Phys. Fluids*, **23**, 1326 (1980).

[3]   C. L. Shepard, J. A. Tarvin, R. L. Berger, G. E. Busch, R. R. Johnson, and R. J. Schroeder, *Phys. Fluids*, **29**, 583 (1986).

[4]   Y. Sakawa, K. A. Tanaka, H. Nishimura, M. Nakai, T. Yabe, H. SakuYai, Y. Izawa, Y. Kato, T. Mochizuki, M. Nakatsuka, and C. Yamanaka, *Phys. Fluids*, **30**, 3276 (1987).

[5]   J. A. Tarvin, G. E. Busch, E. F. Gabl, R. J. Schroeder, and C. L. Shepard, *Laser and Particle beams*. **4**, (3−4), 461−471 (1986).

[6]   H. Figueroa, C. Joshi, H. Azechi, N. A. Ebrahim, and K. G. Estabrook, *Phys. Fluids.* **27** (7), 1887 (1984).

[7]   C. E. Max, Interaction laser−plasma, North−Holland, Physics of the coronal plasma, 345 (1982).

[8]   R. E. Turner and E. A. Williams, UCRL −50021 −86, 3 −24.